RESEARCH ARTICLE

Surface temperatures reveal the patterns of vegetation water stress and their environmental drivers across the tropical Americas

Julia K. Green[1,2] | Ashley Ballantyne[1,3] | Rose Abramoff[1,4] | Pierre Gentine[5,6] | David Makowski[7] | Philippe Ciais[1]

[1]Le Laboratoire des Sciences du Climat et de l'Environnement, CEA CNRS UVSQ, Gif sur Yvette, France

[2]The University of California, Berkeley, California, USA

[3]The University of Montana, Missoula, Montana, USA

[4]Oak Ridge National Laboratory, Oak Ridge, Tennessee, USA

[5]Columbia University, New York, New York, USA

[6]Earth Institute, Columbia University, New York, New York, USA

[7]Institut National de la Recherche Agronomique, University Paris-Saclay, AgroParisTech, UMR 518 MIA, Paris, France

Correspondence
Julia K. Green, Le Laboratoire des Sciences du Climat et de l'Environnement, CEA CNRS UVSQ, Gif sur Yvette, France.
Email: jgreen17@berkeley.edu

Abstract

Vegetation is a key component in the global carbon cycle as it stores ~450 GtC as biomass, and removes about a third of anthropogenic CO_2 emissions. However, in some regions, the rate of plant carbon uptake is beginning to slow, largely because of water stress. Here, we develop a new observation-based methodology to diagnose vegetation water stress and link it to environmental drivers. We used the ratio of remotely sensed land surface to near surface atmospheric temperatures (LST/T_{air}) to represent vegetation water stress, and built regression tree models (random forests) to assess the relationship between LST/T_{air} and the main environmental drivers of surface energy fluxes in the tropical Americas. We further determined ecosystem traits associated with water stress and surface energy partitioning, pinpointed critical thresholds for water stress, and quantified changes in ecosystem carbon uptake associated with crossing these critical thresholds. We found that the top drivers of LST/T_{air}, explaining over a quarter of its local variability in the study region, are (1) radiation, in 58% of the study region; (2) water supply from precipitation, in 30% of the study region; and (3) atmospheric water demand from vapor pressure deficits (VPD), in 22% of the study region. Regions in which LST/T_{air} variation is driven by radiation are located in regions of high aboveground biomass or at high elevations, while regions in which LST/T_{air} is driven by water supply from precipitation or atmospheric demand tend to have low species richness. Carbon uptake by photosynthesis can be reduced by up to 80% in water-limited regions when critical thresholds for precipitation and air dryness are exceeded simultaneously, that is, as compound events. Our results demonstrate that vegetation structure and diversity can be important for regulating surface energy and carbon fluxes over tropical regions.

KEYWORDS
carbon cycle, land surface temperatures, surface energy fluxes, tropical vegetation, vegetation water stress, water cycle

1 | INTRODUCTION

Heat records are increasingly being broken (Seneviratne et al., 2014), resulting in extreme droughts (Zhou, Williams, et al., 2019; Zhou, Zhang, et al., 2019), with dramatic implications for ecosystem services, water resource management, and public health. The ability to predict these events and understand their feedbacks within the climate system is essential for well-informed climate policy that protects vital resources. However, improving the accuracy of climate and carbon cycle predictions requires a better understanding of the climate system, including the role of vegetation in carbon and water cycling.

During photosynthesis, when soil water is abundant, plants lose water from stomata through transpiration, leading to evaporative cooling of the land surface (Bateni & Entekhabi, 2012). In periods of low soil water supply (e.g., low precipitation) and/or high atmospheric water demand (e.g., high vapor pressure deficit; VPD), it is thought that plants close their stomata to varying degrees, in order to maximize carbon gain, while minimizing water loss (Farquhar & Cowan, 1977). Over large regions, gross primary production (GPP) decreases when stomata close due to stress, generating a strong feedback between the water and carbon cycles, and increasing atmospheric CO_2 concentrations (Friedlingstein et al., 2020; Green et al., 2019; Humphrey et al., 2021). In particular, tropical forests store more aboveground carbon than any other ecosystem yet might be vulnerable to water stress (Philipps et al., 2009). As a result, water stress in tropical ecosystems can have large effects on the global carbon cycle and climate (Pan et al., 2011; Spawn & Gibbs, 2020), and an improved understanding of the drivers of vegetation water stress in tropical regions could improve the predictions of the carbon cycle response to drought events.

Additionally, to understand vegetation resilience to water stress in the future, it is essential to be able to identify the causes of water stress (soil vs. air dryness). Although lagged precipitation (used here as a proxy for soil moisture) and VPD are often anticorrelated, they can independently limit photosynthesis and are increasingly becoming decoupled with climate change. In the future, VPD is expected to increase dramatically across the globe, while soil water contents are projected to remain more stable (Zhou, Williams, et al., 2019; Zhou, Zhang, et al., 2019). Thus, depending on their soil water content, ecosystems mostly sensitive to reduced precipitation might be more or less resilient to climate change, while ecosystems more sensitive to VPD might be at higher risk.

Various methods are currently used to identify vegetation water stress. Some of these rely on process-based models, which depend on the accuracy of the model forcing data, as well as the underlying assumptions and parameterizations used in the model (e.g., the Global Land Data Assimilation System; Rodell et al., 2004). Some methods rely on precipitation data only and do not take into account atmospheric demand, which however regulates terrestrial water storage through evapotranspiration (e.g., the standardized precipitation index; McKee et al., 1993). Other methods use model estimates of evapotranspiration (ET) to take into account the impact of water demand (e.g., cumulative water deficit; Aragão et al., 2007); however, while ET can be directly measured at the ecosystem scale, it can only be indirectly estimated at the regional scale by models, with difficult-to-constrain assumptions, resulting in high degrees of uncertainty, especially during stress periods (Long et al., 2014; Sörensson & Ruscica, 2018). Other studies have used vegetation indices, which tend to saturate in the tropics (Huete et al., 1997), or have used solar-induced fluorescence (SIF), which has been shown to continue to increase in the Amazon even while stomatal conductance is decreasing in response to atmospheric water stress (Green et al., 2020). Other techniques exist such as examining water stress using soil moisture data (Feldman et al., 2019; Liu et al., 2020), yet soil moisture suffers from a lack of observations for the full soil profile that may integrate decoupling between surface and root zone soil moisture (Qiu et al., 2016), and it is difficult to observe in dense biomass regions. Additionally, although these methods were designed to identify stress occurrence, they are not able to reveal the causes of stress, and to rank them according to their importance. Thus, there is a need for a simple and direct stress indicator to diagnose vegetation water stress, as well as a robust methodology linking vegetation water stress to environmental drivers and plant production in a spatially explicit way.

Here, we study vegetation water stress in the tropical Americas, derived from globally available and directly measurable remotely sensed data: namely, land surface (skin) and near surface air temperature datasets. The approach is based on the surface energy budget (Equation 1), where net radiation (R_n) is equal to the fluxes of ET, sensible heat flux (H), and the ground heat flux (G), which is considered to be small, such that:

$$R_n = ET + H + G \qquad (1)$$

ET and H are inversely related (Equation 1), whereby due to strong evaporative cooling, H tends to increase with increased R_n and decrease with increased ET (Bateni & Entekhabi, 2012). Thus, accounting for changes in R_n, and assuming that G is negligible, changes in ET will lead to changes in H. Therefore, we can exploit the gradient between land surface temperature (i.e., the radiative skin temperature of the land surface; LST) and near surface air temperature (T_{air}) as a direct constraint on H and a quantitative measure of vegetation water stress (Equation 2), where ρ is the density of air, c_p is the specific heat of air, and r is the compound aerodynamic resistance from the air, soil, and vegetation.

$$H = R_n - ET = \rho c_p \frac{(LST - T_{air})}{r}. \qquad (2)$$

Both LST and T_{air} temperature datasets are available globally from remote sensing platforms, and have been validated using remote sensing, reanalysis, and station data; however, it should be noted that stations in tropical regions for ground validation are very limited, and due to cloud coverage, these regions can have lower accuracy with their measurements than surrounding regions. While

many factors contribute to the aerodynamic resistance term (e.g., canopy height, leaf area index, etc.) making it difficult to constrain, in principle LST-T_{air} provides a sensitive proxy of sensible heat. The ratio of these temperature datasets, which reflects similar behavior to LST-T_{air} (correlation >.98 throughout the study area), can also be used as a proxy for sensible heat (such that LST/T_{air} values greater than 1 indicate positive sensible heat fluxes from the surface to the atmosphere and values less than 1 indicate negative sensible heat fluxes due to evaporative cooling).

While variability in LST/T_{air} can be due to factors other than water stress (e.g., radiation, changes in biomass, foliage area, or land cover change), if one is able to account for these other factors, the contrast between these temperature datasets (both measured in Kelvin) has the potential to be used for monitoring vegetation water stress and resilience to drought in near real time. Thus, while previous studies have investigated variations between these datasets to understand and explain their regional patterns and the relationship between LST and T_{air} (Good, 2016; Lian et al., 2017), this study goes further to investigate the sensitivity of stress, as indicated by LST/T_{air}, to environmental drivers, their thresholds, ecosystem attributes that may mediate these thresholds, and their impacts on primary productivity, as guided by the following research questions:

1. What is the sensitivity of LST/T_{air} to radiation (both net radiation and the fraction of shortwave diffuse radiation) as opposed to soil dryness (i.e., lagged precipitation) and air dryness (i.e., VPD)?
2. What are the ecosystem attributes that underpin regions where LST/T_{air} is distinctly controlled by radiation, precipitation, or VPD?
3. Are there local precipitation and VPD critical thresholds, which when crossed result in a sharp increase in LST/T_{air}, indicating predominant water stress?
4. When such thresholds in water supply or demand are exceeded, how are photosynthetic rates (i.e., GPP) impacted?

These four questions are addressed by training two different machine learning algorithms. Question 1 is addressed using pixelwise fitted random forests (RFs) on 8-day LST/T_{air} time series as the response variable, and climate drivers that can change the surface energy budget as predictor variables (Figure 1: Boxes 1 and 2a). We then use these results to explain the regional patterns of the dominance of each climate driver by soil and vegetation attributes, this time using regional RF models to address Question 2 (Figure 1: Boxes 3a and 4a). Next, we combine the results of our pixelwise RF models (used to address question 1) with Shapley values and piecewise linear functions to quantify critical stress thresholds, addressing Question 3 (Figure 1: Box 2a). Lastly, we use *GPP* data with the critical thresholds defined in Question 3, to investigate *GPP* responses to water stress, addressing Question 4 (Figure 1: Boxes 2b and 2c). Although we focus this analysis on the tropical Americas because of the region's large impact on the global climate, our methodology is generic and can be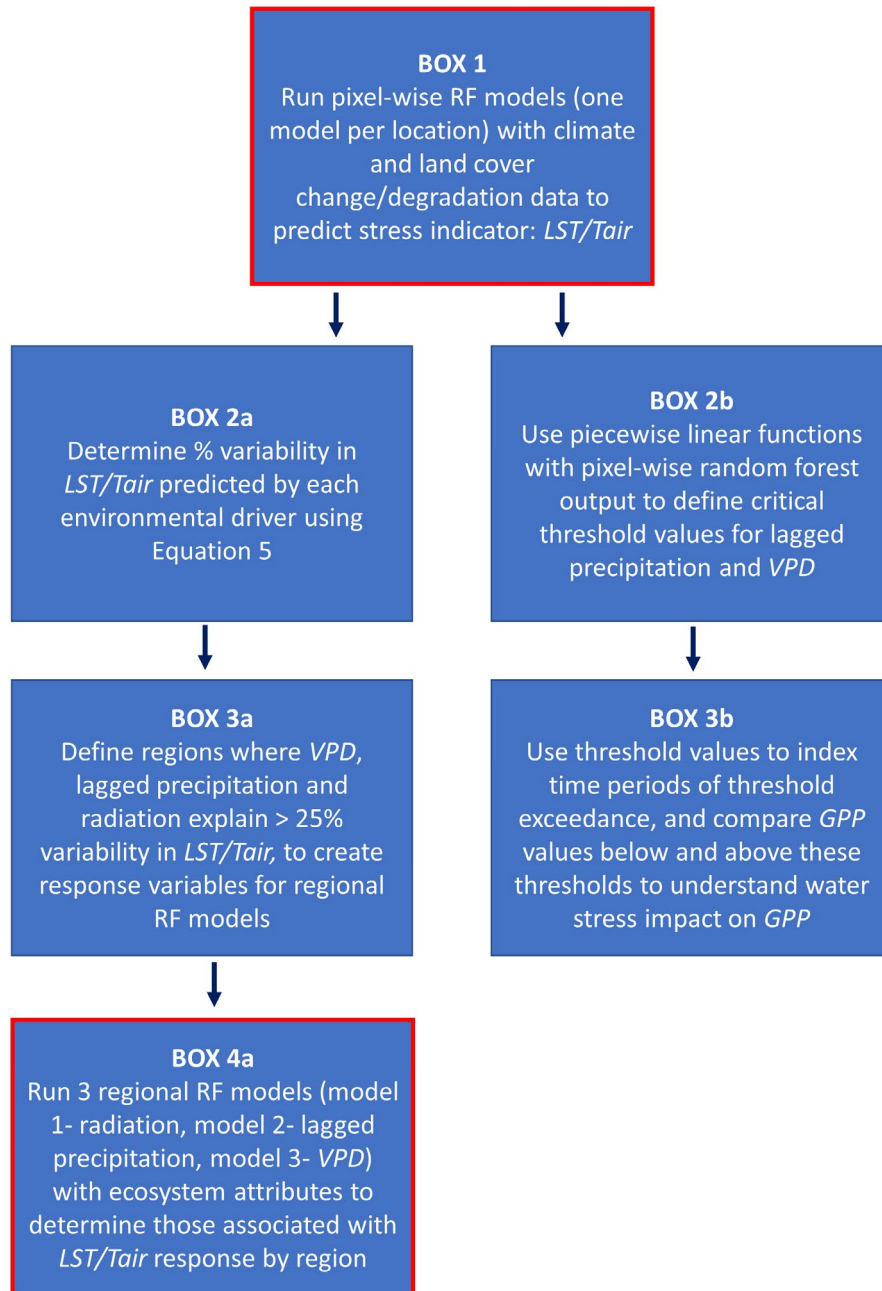 applied to other regions or global datasets, with the potential to improving understanding of carbon and energy fluxes.

2 | MATERIALS AND METHODS

Land surface temperatures (e.g., LST) as observed near-continuously by satellites over vegetated surfaces reflect the temperature of the top of the canopy. LST varies due to groundcover or ecosystem type, radiation, clouds, wind conditions, and the amount, type, and status of vegetation present. Most importantly for this application, LST is related to the surface energy budget and to the rate of evaporative cooling (Bateni & Entekhabi, 2012). While T_{air} is directly affected by R_n, clouds, and H due to land-atmosphere feedbacks, T_{air} changes tend to be reduced and less extreme compared to LST (Gentine et al., 2016; Good, 2016). Therefore, changes in the ratio of LST to T_{air} contain valuable information on vegetation stress, whereby increasing LST/T_{air} is indicative of increased H due to water stress (i.e., decreased ET due to decreased evaporative cooling from reduced surface conductance) for a given radiation level, decreasing LST/T_{air} is indicative of decreased H and reduced water stress (i.e., increased ET), and a value <1.0 indicates evaporative cooling of the atmosphere. However, changes in LST/T_{air} can also occur due to other environmental conditions (e.g., radiation, from increased energy not being entirely dissipated through transpiration), and so it is necessary to be able to quantify the LST/T_{air} variability due to water stress versus other factors to effectively use LST/T_{air} to understand vegetation status.

2.1 | Pixelwise random forest models

To address our first research question, we applied RFs (one model per half-degree by half-degree pixel location) to predict the computed LST/T_{air} time series, using a suite of environmental variables as predictors to determine the variability in the LST/T_{air} time series due to water stress versus other factors (Figure 1: Box 1; Table S1). For T_{air}, near surface data from the Atmospheric Infrared Sounder (AIRS) platform (Teixeira, 2013) located aboard the NASA AQUA satellite (daily 1:30 pm local overpass time, assumed to be ~maximum T_{air}) were used. These data were extrapolated from the temperature measurements from the nearest atmospheric pressure level and the surface, and thus represent an average air temperature value in the layer of the atmosphere closest to the surface. For LST, hourly data from geostationary satellites in the Copernicus program (Martins et al., 2020) were used. From the daytime hours (10 am to 4 pm local time), the maximum LST was taken to create daily data. Geostationary satellite LST data products represent a breakthrough because they can capture the strong diurnal cycle in LST, which directly reflects surface energy partitioning and water stress. Additionally, in cloudy regions such as the tropics, hourly data allow for a higher frequency of clear sky observations than once-a-day data (hence why the maximum value of the available daytime hourly data was used in lieu of

BOX 1
Run pixel-wise RF models (one model per location) with climate and land cover change/degradation data to predict stress indicator: *LST/Tair*

BOX 2a
Determine % variability in *LST/Tair* predicted by each environmental driver using Equation 5

BOX 2b
Use piecewise linear functions with pixel-wise random forest output to define critical threshold values for lagged precipitation and *VPD*

BOX 3a
Define regions where *VPD*, lagged precipitation and radiation explain > 25% variability in *LST/Tair*, to create response variables for regional RF models

BOX 3b
Use threshold values to index time periods of threshold exceedance, and compare *GPP* values below and above these thresholds to understand water stress impact on *GPP*

BOX 4a
Run 3 regional RF models (model 1- radiation, model 2- lagged precipitation, model 3- *VPD*) with ecosystem attributes to determine those associated with *LST/Tair* response by region

FIGURE 1 A flow chart of the study methodology. Boxes outlined in red reflect steps using pixelwise random forest (RF) models (Box 1) and regional (categorical) RF models (Box 4a)

LST measured at 1–2 pm, which would reduce the number of measurements available). It should be noted that on certain days, the LST value used may not reflect the true daily maximum due to cloud coverage preventing measurements for each hour of the day, but we use it to reflect the time of greatest potential vegetation stress. Both datasets were brought to an 8-day temporal resolution by taking the median value of each 8-day period, so that detecting droughts or heat waves that occur on short timescales ("flash" events) were possible, but were long enough to average out noise due to short-term daily weather variability. The datasets were brought to a half-degree spatial resolution, and span from 2011 to 2019. At the global scale, LST/T_{air} is >1.0 on mean annual timescales because daytime H is positive. However, over certain regions or seasons, it is possible that LST/T_{air} is <1.0 as a result of evaporative cooling of the vegetation

surface, or because of the presence of cold air advection (Fig. S1). It should also be noted that both datasets have some degree of bias associated with them due to their retrievals. However, for this analysis, we are less concerned with the absolute values of LST/T_{air}, and instead focus on temporal changes in the relative ratio for every location. Thus, systematic biases for particular regions should be limited when using this indicator.

For predictors in the pixelwise RF models, we chose variables that are related to both climate and land cover, as they would influence surface energy fluxes. For radiation, we used R_n, calculated from incoming and outgoing surface shortwave and longwave radiation from the Clouds and the Earth's Radiant Energy System (CERES; Wielicki et al., 1996), and the fraction of shortwave diffuse radiation calculated from the shortwave direct and diffuse radiation from

CERES. For soil water stress, precipitation data from the Tropical Rainfall Measuring Mission (TRMM; Huffman et al., 2007) data were used at time lags of 0, ~1 month (four 8-day timesteps) and ~2 months (eight 8-day timesteps); lagged data were used to account for the memory of soil moisture, which integrates several months of precipitation anomalies. Lagged precipitation data were used in lieu of soil moisture data due to the lack of soil moisture measurements throughout the root zone under dense canopy (Souza et al., 2018), and issues with remote sensing surface soil moisture data accuracy in dense forest (Entekhabi et al., 2014). It should be noted that the analysis was also performed using a computed cumulative water deficit dataset as a predictor in lieu of lagged precipitation, which yielded similar results. Related to air dryness stress, VPD was calculated using AIRS relative humidity (RH) and T_{air} using the Clausius–Clapeyron relationship (Equation 3), where e_o is the integration constant, L_v is the latent heat of vaporization, R_v is the vapor gas constant, and T_o is a second integration constant. Both T_{air} and RH are measured in the early afternoon (1:30 pm local overpass time).

$$\text{VPD} = e_o * \exp\left[\frac{L_v}{R_v} * \left(\frac{1}{T_o} - \frac{1}{T_{air}}\right)\right] * \left(1 - \frac{RH}{100}\right). \quad (3)$$

For other climatic factors, mean surface wind, calculated from the u- and v-components of ERA5 data (Dee et al., 2011), and

vegetation phenology, calculated as the climatology of clear-sky instantaneous contiguous solar-induced fluorescence (CSIF; Zhang et al., 2018), were also used as predictors. CSIF has been shown to be nearly linearly related to *GPP* at the spatial and temporal scales used in this study (Zhang et al., 2018), thus by using the climatology of CSIF in lieu of the raw data, we are able to smooth out the effects of stress events on the signal of GPP, and instead account for seasonal climatological changes in vegetation phenology. All datasets were brought from their native resolutions to 8-day temporal, and half-degree spatial scales, and a cubic spline algorithm was applied with a smoothing parameter of 0 to remove noise (Wuertz, 2020; Figure 2a). Since these datasets were being used to look at vegetation stress, only growing season data were used, defined as the timesteps when the climatology of CSIF was >0.3 times the maximum CSIF climatology. It should be noted that due to difficulty in measuring roughness at the scale necessary (related to aerodynamic resistance), these data were not included as a predictor in the models, although wind data and phenology, which are related to roughness, are included.

Land cover is an important driver of the surface energy budget, and thus of LST/T_{air}, because certain land cover types (e.g., tropical forests) have a greater ability to transpire water than others (e.g., savannas). For predictors related to land use and land cover change, gridded MODIS annual land cover data from 2011 to 2019 were used
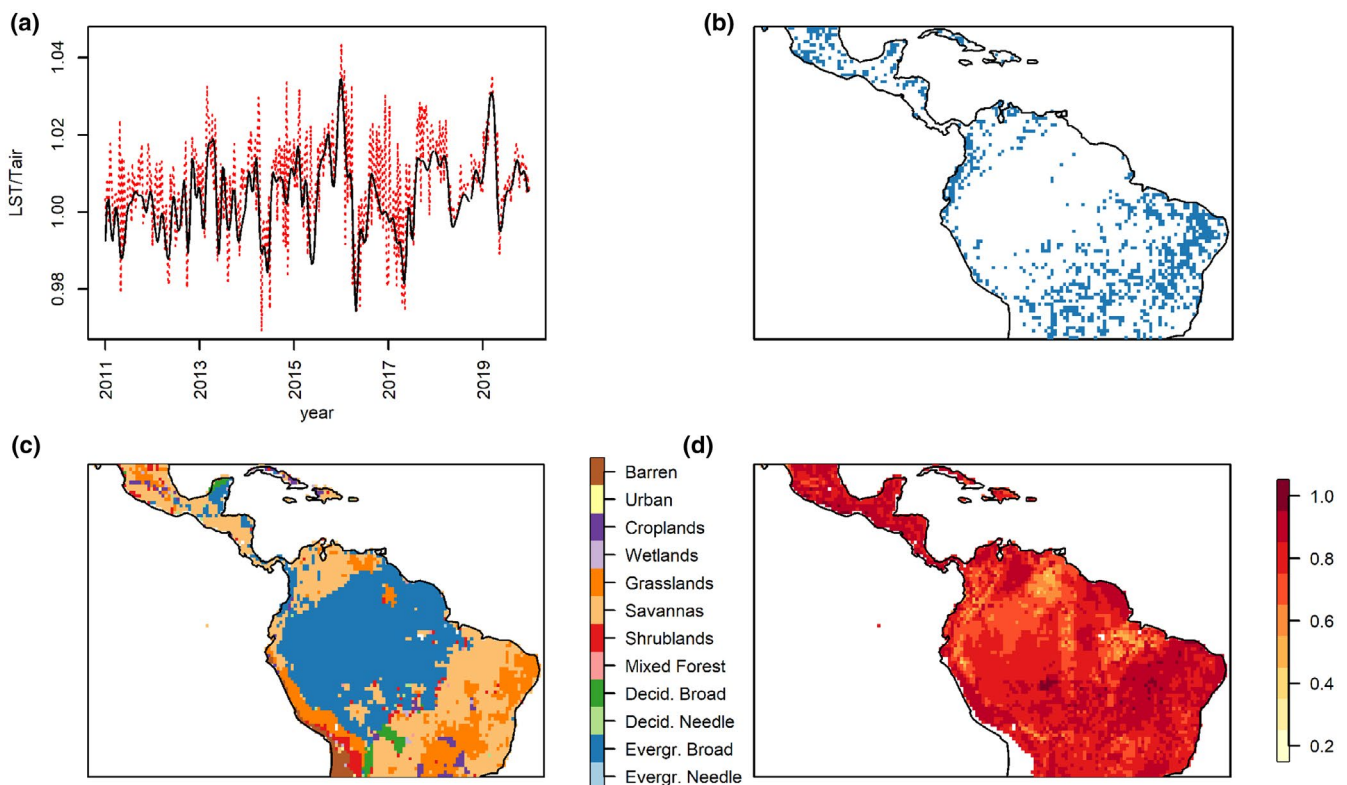
FIGURE 2 The time series of land surface temperature versus near surface air temperature (LST/T_{air}) from a sample pixel for the time period 2011–2019 smoothed using a cubic spline (black line) and unsmoothed (red dashed line) (a). Pixels that were defined as having land cover change of at least 10% in the time period of 2011–2019 based on MODIS land cover data (b). The primary land cover type per pixel for 2015 (c). R-squared values for the pixelwise random forest models used to predict time series of LST/T_{air} (d).

(Friedl & Sulla-Menashe, 2018). The 17 land cover types defined by the University of Maryland classification scheme were merged into a subset of nine (Table S2), and an individual predictor variable was created for each one of these merged classes. To generate the time series of percent change in land cover type in a half-degree by half-degree grid cell, first the 100 MODIS 0.05 by 0.05-degree pixels of the top land cover class from 2011 was compared with these same 100 pixels from 2019. Should a land cover type change by more than 10% (10/100 pixels) over this time period, then the annual data from 2011 to 2019 were linearly interpolated to an 8-day temporal resolution for that land cover class in that grid location. Should a land cover type change by <10%, then the change was attributed to uncertainty in land cover class labels at the 500-m MODIS spatial resolution, and a constant mean percent land cover class value was reported for each timestep of that location. Regions where land cover changed by more than 10% between 2011 and 2019 are displayed in Figure 2b, and the predominant land cover type per pixel for the middle of our study period (2015) is displayed in Figure 2c.

RFs were constructed for each pixel time series within the study region using the "ranger" package in R (Wright & Ziegler, 2017; Figure 1: Box 1). RFs are relatively simple machine learning models based on regression trees that have high performance with limited problem of overfitting. They do not make assumptions about underlying data distributions or variable relationships, and they tend to retain high performance even with interactions between independent predictors (Breiman, 2001). Additionally, their results can be used to construct partial dependence plots (PDPs; Greenwell et al., 2018) and calculate Shapley values, and thus analyze the sensitivity of the output to the input variables, and improve upon feature importance. Shapley values decompose LST/T_{air} anomalies (i.e., each deviation expressed as the difference between an individual prediction and the mean predictions of the model) into several components measuring the contributions of the inputs to the anomaly (Hart, 1989). They are based on game theory and are useful for disentangling near collinearities in the data, allowing deeper analysis of correlated features for the identification of vegetation stress drivers and thresholds.

Predictor variables with low predictive power were removed from the RF models. For each pixel location, first, an RF model was run with all predictor variables included, and the predictor variables were ranked according to their permutation importance. The model was then rerun, with the least important variable removed from the model, a process called recursive feature elimination (RFE; Guyon et al., 2002). Importance values were then recalculated and stored, and this process was repeated until the three most important predictor variables remained in each pixel's model. From here, the R-squared value was tabulated based on the out-of-bag (OOB) observations (~one-third of the observations; Breiman, 2001), and then, the model was rerun with the next most important variable added back in (based on the importance rankings stored during RFE). The R-squared value of this model based on the OOB observations was then retabulated, and should the R-squared value increase by at least .005, the predictor variable remained in the model (otherwise, it was removed) and the next most important variable was then

added back into the model and was rerun with a new R-squared value tabulated. This process was repeated until all predictor variables had been added back into the model, and the variable combination with the highest OOB R-squared value was selected for the final model. Additionally, for each model, the number of variables used at each node split (between 2 and the number of predictor variables) and the number of trees used in the model (between 50 and 1000) were optimized to have the greatest OOB R-square value (the median number of trees selected was 450). In this way, the best quality model could be developed by only including the most informative inputs.

2.2 | Spatial variability

While variable importance in RF models can be useful in terms of eliminating unnecessary predictor variables from a model and understanding variable relationships, this quantity does not reveal how a predictor variable influences the temporal variance of the stress indicator. Therefore, Shapley values were calculated using the R-package "fastshap" (Greenwell, 2020) based on each pixel's RF model for all predictor variables using 25 simulations. A Shapley value greater (less) than 0 indicates that for a particular timestep, the predictor variable is pushing LST/T_{air} above (below) the mean value of its time series. Therefore, the percentage of variability explained in LST/T_{air} by each predictor variable (% var $\left(\frac{LST}{Tair}\right)$) could be calculated by combining the importance of each predictor variable, calculated from the average absolute value of the Shapley values (Hart, 1989; Equation 4; where $X_{1,imp}$ is the importance of the environmental predictor X_1, $X_{1,SHAP}$ is the vector of generated Shapley values (one per timestep) for predictor X_1, ts is the timestep, and n is equal to the total number of timesteps in the time series), with the OOB R-squared value (Figure 2d; Equation 5).

$$X_{1,imp} = \frac{\sum_{ts=1}^{n} |X_{1,SHAP}|}{n} \quad (4)$$

Equation 5 provides an example of the percent variability explained in LST/T_{air} by predictor X_1, where i is the total number of predictors:

$$\% \text{ var} \left(\frac{LST}{T_{air}}\right) X_1 = 100 R^2 \frac{X_{1,imp}}{X_{1,imp} + \ldots + X_{i,imp}}. \quad (5)$$

Using these results, maps were created that showed the average contributions of each environmental variable to changes in LST/T_{air} (Figure 1: Box 2a; Figure 3).

While importance values do not provide information about whether the predictor variable has a positive or negative influence on the response variable, the average effect is defined as being positive or negative in Figure 3 based on the variable relationships depicted in the Shapley dependence plots (Figure 4a). Should the Shapley values positively (negatively) correlate with the predictor variable, this

FIGURE 3 The percent variability in land surface temperature versus near surface air temperature (LST/T_{air}) determined via random forest models explained by net radiation (R_n) (a), the fraction of diffuse shortwave radiation (b), the sum of current and lagged precipitation (c), and vapor pressure deficit (VPD) (d). Positive (negative) values represent regions where an environmental driver tends to increase (decrease) LST/T_{air}. Regions where at least 25% of the LST/T_{air} variability is driven by radiation (the sum of the absolute values of subplots [a] and [b]) (e), where at least 25% of the LST/T_{air} variability is driven by current and lagged precipitation (f), and where at least 25% of the LST/T_{air} variability is driven by VPD (g). Country borders are depicted with black lines
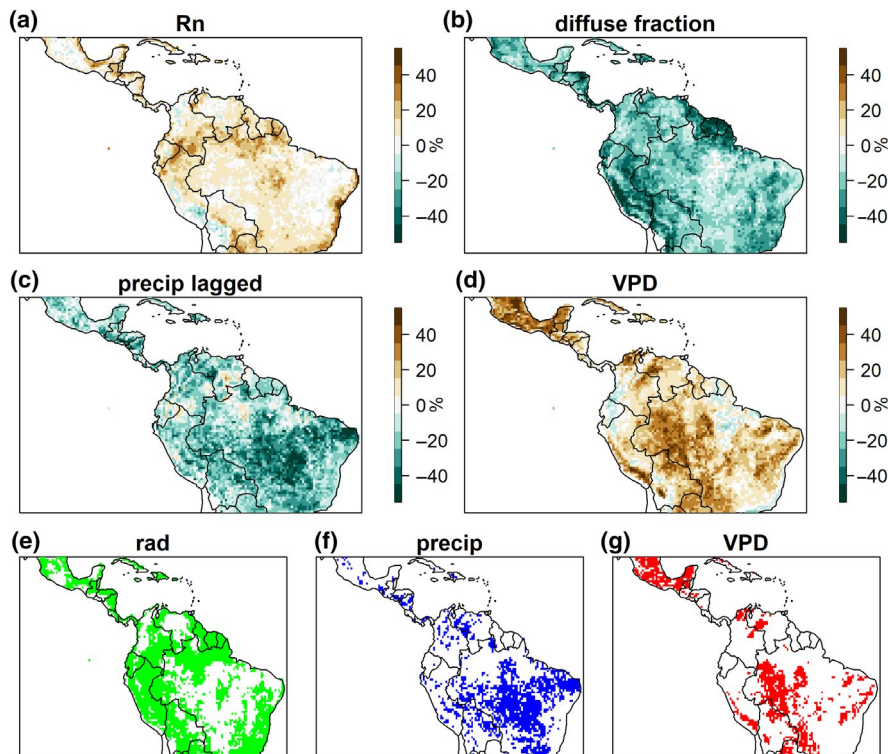
FIGURE 4 A sample pixel Shapley dependence plot showing the Shapley values for vapor pressure deficit (VPD) used to predict land surface temperature versus near surface air temperature (LST/T_{air}) (a) and the partial dependence plot of the predictions of LST/T_{air} on VPD from the random forest model (b). The red point at the highest x-value represents the critical threshold value for VPD at this location generated via the best-fit piecewise linear function
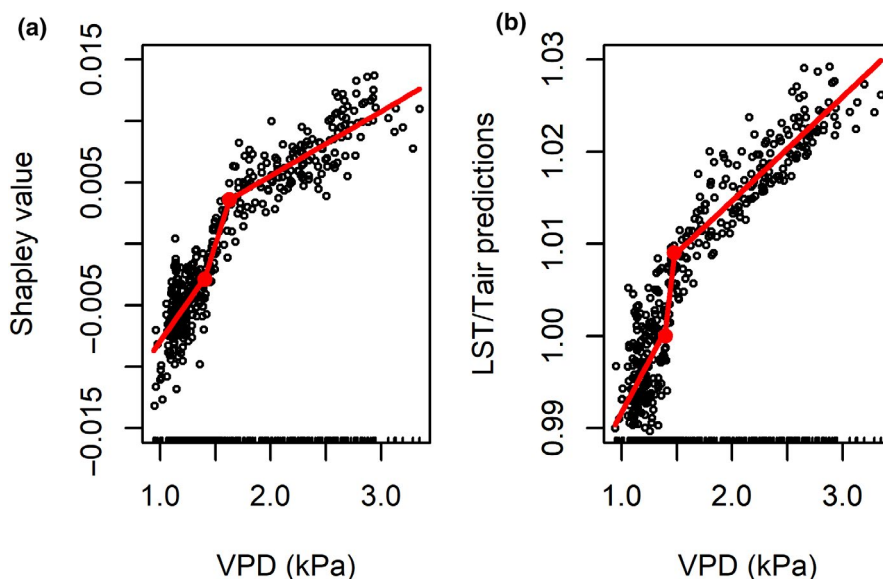
is defined as a positive (negative) influence. As a check, the PDPs from the RF models, which depict the prediction function between each predictor variable and the response variable (Greenwell, 2017; Figure 4b), were also used. Very similar results were obtained, emphasizing the consistency between the two methods.

2.3 | Regional random forest models with ecosystem attributes

While the pixelwise random forest models reveal that the surface energy budget is primarily regulated by radiation (R_n and the fraction

of diffuse shortwave radiation) as well as water supply and demand, they do not provide information on why a region might have its surface energy fluxes modified by one climactic influence over another. Thus, to understand the ecosystem attributes associated with spatial variations diagnosed from the pixel-wise RF models and answer our second research question, three regional RF models were used to classify where LST/T_{air} variability is driven by radiation, lagged precipitation (soil moisture), and/or VPD (Figure 1: Boxes 3a and 4a).

The first model distinguished pixels where LST/T_{air} was strongly driven by radiation (defined as having at least 25% of the variability in the LST/T_{air} time series explained by the linear sum of the absolute value of the percent variability explained in LST/T_{air} by the diffuse

shortwave fraction and R_n) versus pixels not strongly driven by radiation (Figure 3e). The second model distinguished where LST/T_{air} was strongly driven by precipitation limitation (at least 25% of the variability in LST/T_{air} explained by the linear sum of the absolute values of the percent variability in LST/T_{air} explained by the linear sum of precipitation at 0, 1-month and 2-month lags) versus not strongly driven by precipitation limitation (Figure 3f). The third model distinguished where LST/T_{air} was strongly driven by *VPD* limitation (at least 25% of the variability in LST/T_{air} explained by *VPD*) versus not strongly driven by *VPD* (Figure 3g). Thus, these three categorical RF models were trained to classify these different situations using inputs related to ecosystem attributes affecting resistance (Equation 2).

For ecosystem attributes, variables were selected to describe the variability in rainfall (known to effect vegetation structure and resilience [Holmgren et al., 2013]), soil properties, and vegetation aboveground and belowground structure. In addition to climate, these types of ecosystem attributes have been shown to affect vegetation resistance to drought (Holmgren et al., 2013; Quesada et al., 2012) due to their impact on nutrient availability, the retention of water in the soil, and the ability of plants to access it. For rainfall variability, we used the standard deviation of 8-day precipitation data, which reflects the seasonal and interannual variability of rainfall. While this was included in the initial models, it was later omitted to constrain the analysis to include only those variables that were less directly related to climate. For soil properties, we considered phosphorus content (Yang et al., 2013; an important nutrient for photosynthesis [Quesada et al., 2010, 2012]); the cation exchange capacity of the clay fraction (CECC; related to the ability of clay to retain water in the soil); the pH of the soil water (related to plant nutrient availability); the bulk density, silt content, clay content, sand content, and gravel content (all related to the infiltration of water through the soil); and area-weighted soil organic carbon content (SOC; which increases soil fertility). These data products are from the Harmonized World Soil Database version 1.2 (FAO/IIASA/ISRIC/ISSCAS/JRC, 2012; Wieder et al., 2014) and are regridded by the Oak Ridge National Laboratory (FAO/IIASA/ISRIC/ISSCAS/JRC, 2012; Wieder et al., 2014). While these soil properties are broken into their topsoil (0–30 cm) and subsoil (30–100 cm) components, these values tend to be highly correlated (>.95); thus, they were combined $(0.3 \times \text{topsoil} + 0.7 \times \text{subsoil})$ to reflect the average top 1 m of the soil column.

For vegetation structure, we considered aboveground biomass (AGB; Saatchi et al., 2011; related to canopy light availability and humidity), leaf area index (LAI; related to drought resilience and aerodynamic resistance), tree height (related to forest susceptibility to VPD vs. precipitation; Giardina et al., 2018), tree stand density (related to soil water availability), maximum rooting depth (Fan et al., 2017; related to plant access to soil water), elevation (related to vegetation structure and mean temperature), species richness (Ellis et al., 2012; related to a greater diversity of plant hydraulic traits), and the primary land cover type (Friedl & Sulla-Menashe, 2018) from 2015 (the middle year of the study period). Species richness was normalized

for each location as the species richness divided by the maximum species richness in the study area. Although variables describing vegetation structure such as AGB and species richness can be related to rainfall, it should be noted that they have their own distinct patterns demonstrating that forest structure can vary even when regions share similar rainfall patterns (Figs S2 and S3). Predictor variables that had correlations >.7 with one another were removed; thus LAI, tree height, and tree stand density were ultimately excluded from the analysis due to their high correlations with AGB, and their lower importance relative to AGB (determined using RFE). All utilized predictors in the final models are displayed in Fig. S2.

Similar to the pixelwise RF models, RFE was implemented to ensure that only predictors contributing to reducing the prediction error were included in the final model; for these models, the model performance was evaluated based on the OOB prediction error (defined as the percentage of misclassified samples in these categorical models). For all three models, 20 simulations were performed using different seed values, and the most commonly occurring selection of predictor variables was selected. Then, 10 simulations with different seed values were run for each of the three models using the final combination of predictor variables. The most important variables for each model were determined based on the most reduced model generated during RFE (a model with only two predictors), and the Shapley dependence plots and maps (Figure 5) are based on the average of these 10 simulation results.

As was done with the initial RF models run per pixel, for each regional RF model simulation, the number of variables to be used at each node split (between 2 and the number of predictor variables) and the number of trees used in the model (between 50 and 1000) were optimized to minimize prediction error. However, unlike the previous RF models, the response variable was categorical (i.e., in the VPD model, the response variable was 1 when VPD explained at least 25% of the variability in LST/T_{air}, and was 0 for when it did not). Thus, for the final RF model, a framework was used that produced results that described the probability of being categorized as having stress controlled by VPD, lagged precipitation, or radiation.

2.4 | Critical hydroclimatic thresholds and GPP

To identify critical hydroclimatic thresholds and sensitive regions and answer our third research question, Shapley dependence plots were used to examine the nonlinear relationship between predictors and Shapley values from the original pixelwise RF models (Figure 1: Box 2b; Figure 4). It is possible that, for example, vegetation may not be stressed at low VPD values, but that once a certain *VPD* value is exceeded (a threshold), vegetation may become stressed, indicated by a sudden increase in LST/T_{air}. Similarly, thresholds will exist between current and lagged precipitation and our stress indicator. These threshold values were pinpointed for all locations that had a positive correlation >.1 between LST/T_{air} and VPD, and <−.1 between LST/T_{air} and lagged precipitation, using linear piecewise functions with one to two break points
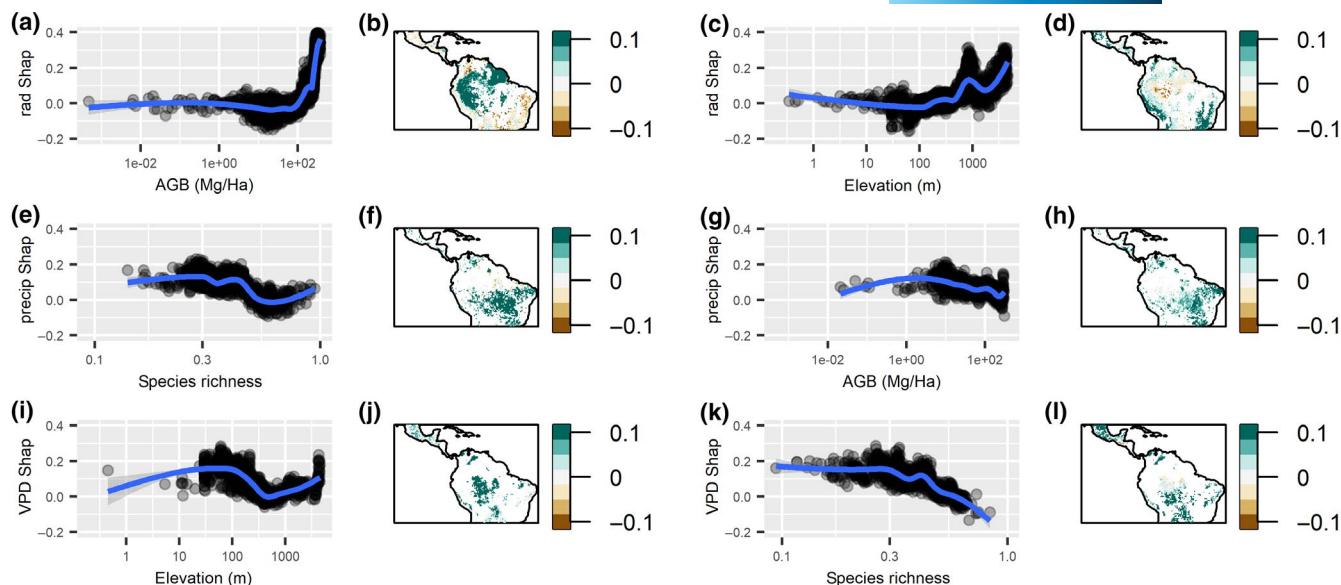
FIGURE 5 The two most important variables determined via regional random forest models that contribute to the probability of a region being radiation dominated (a–d), precipitation dominated (e–h), and vapor pressure deficit (VPD) dominated (i–l). Subplots (a), (c), (e), (g), (i), and (k) are partial dependence plots created using Shapley values, while subplots (b), (d), (f), (h), (j), and (l) show the corresponding maps for each Shapley value location. Only pixels where at least 25% of the variability in land surface temperature versus near surface air temperature (LST/T_{air}) is explained by radiation (top row), precipitation (middle row), and VPD (bottom row) are displayed

FIGURE 6 Critical threshold values determined using linear piecewise functions with Shapley value partial dependence plots computed from random forest models of land surface temperature versus near surface air temperature (LST/T_{air}) time series for current precipitation (a), precipitation with a 1-month lag (b), and precipitation with a 2-month lag (c), and vapor pressure deficit (VPD) (d). Precipitation data are in units of mm/d and VPD is in units of kPa
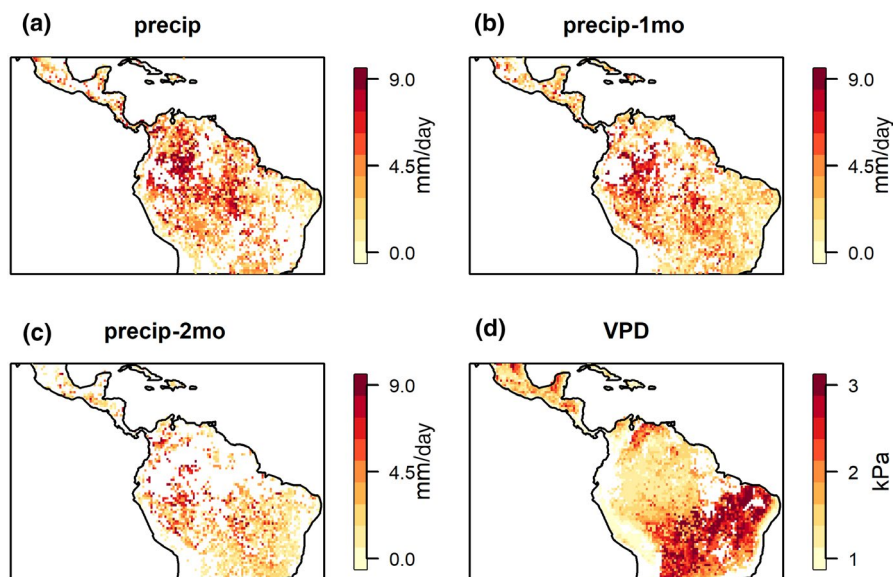
(relationship dependent). For VPD, the threshold was defined as the greatest breakpoint value of the piecewise linear function fit to the Shapley dependence plot, and for the precipitation variables, it was the lowest breakpoint (Figure 4). Maps were created to visualize how the thresholds for lagged precipitation and VPD change across different ecosystems (Figure 6).

To answer our fourth research question, we used the pixelwise critical threshold values defined via the Shapley dependence plots (Figures 4 and 6) to index time periods when lagged and current precipitation values were simultaneously above their critical thresholds, and VPD was below its critical threshold (indicating our baseline period of no stress). For each pixel, we then indexed time periods when

there was only precipitation stress (both precipitation and VPD were below their critical thresholds), only VPD stress (both precipitation and VPD were above their critical thresholds), and when there was both precipitation and VPD stress (precipitation was below its critical threshold, and VPD was above its critical threshold). Then, using GPP data from FLUXCOM RS (Jung et al., 2020), the average daily GPP during time periods without stress (our baseline) were compared to periods of only precipitation stress, only air dryness stress, and periods of simultaneous precipitation and VPD stress (Figure 1: Box 3b; Figure 7). In this way, we could understand how GPP in this region is being affected by both VPD and lagged precipitation when these thresholds are crossed both separately and concurrently. This

analysis was also repeated using CSIF data as a proxy for *GPP*, which confirmed similar patterns of carbon uptake changes associated with variations in LST/T_{air}. Nevertheless, it should be noted that both the threshold values and the FLUXCOM *GPP* data are the products of statistical regression models, and thus, there is some uncertainty associated with these final values due to the model assumptions, especially during extremes when the model is less skillful (Jung et al., 2020). It should be noted that FLUXCOM is known to underestimate the interannual variability of *GPP* (Jung et al., 2020).

3 | RESULTS

3.1 | LST/T_{air} sensitivity to environmental drivers

We found that radiation generally controls the variations of LST/T_{air} in wetter regions; however, the specific relationship changes regionally. R_n is positively associated with LST/T_{air} in very wet regions where radiation is limiting, such as the northern sections of the Amazon rainforest and the Guyana shield, as well as the southeastern Atlantic Forest (Figure 3a). Meanwhile, increases in the fraction of diffuse shortwave radiation reduce LST/T_{air} throughout the study region, with the largest influence in the Guiana Shield and the Andes Mountains (Figure 3b). Summed together, radiation explains over 25% of the temporal variability in 8-day LST/T_{air} in ~58% of this study area (Figure 3e).

Both current and lagged precipitation (from 1 and 2 months prior) as indicators of water supply are high when LST/T_{air} is low (and vice versa), except in a few small regions of the Amazon Rainforest (Figure 3c). Its impact is the smallest in the Amazon rainforest, and then increases on the forest edges as it transitions to savanna and becomes drier. Summed together, lagged precipitation explains over 25% of the variability in LST/T_{air} in ~30% of the study area (Figure 3f). In certain regions such as the Central and Eastern regions of Brazil, as much as 30%–40% of variability in LST/T_{air} is explained by precipitation (Figure 3c).

We found that VPD is positively associated with LST/T_{air} throughout the study region indicating widespread vegetation stress from atmospheric dryness (Figure 3d). This is particularly seen in regions including tropical rainforest, savanna, and grassland. VPD explains over 25% of the temporal variability in LST/T_{air} in ~22% of the study area (Figure 3g). Its signal is strongest in the center and southwest regions of the Amazon rainforest of Brazil, the savanna of northern

Paraguay, Bolivia and Brazil, and Southern Mexico. Its effect diminishes in the northern section of the Amazon rainforest and switches to a slightly negative relationship with LST/T_{air} in the wet and colder Andes mountains in the northwest of South America, as well as the wet region surrounding the mouth of the Amazon River.

While the sensitivity of LST/T_{air} to radiation, lagged precipitation, and air dryness is spatially clustered in specific regions, there are also often transitional zones between these areas, where two drivers can explain more than 25% of the variability in LST/T_{air}. These overlapping regions cover 10% of the study region for radiation and lagged precipitation (mainly in the southeast of Brazil), 8% for radiation and VPD (in parts of the Amazon and Central America), and 5% for lagged precipitation and VPD (mainly in the savanna southeast of the Amazon rainforest). It is extremely rare for all three climate variables to be of importance in the same location (Figure 3e–g).

3.2 | Ecosystem attributes that control spatial patterns of LST/T_{air} sensitivity

In regions where at least 25% of LST/T_{air} variability can be explained by the fraction of shortwave diffuse radiation and R_n, the corresponding ecosystem attributes ranked from most to least important are AGB, elevation, species richness, soil water pH, the cation exchange capacity of the clay (CECC), root depth, soil gravel content, and soil organic carbon (SOC). Radiation-dominated regions can thus be characterized most accurately using AGB and elevation, and radiation becomes increasingly important at both high AGB of the Amazon rainforest and at higher elevations along the Atlantic Coast and the Andes (Figure 5a–d).

In areas where increasing LST/T_{air} is strongly positively associated with lagged precipitation, indicating water stress from water supply, the ecosystem attributes that are most important are species richness, AGB, soil water pH, CECC, root depth, soil gravel content, and soil clay content. Of these predictors, species richness and AGB are the top two predictors. In regions of low species richness, outside of the rainforest regions, there is a greater likelihood that there will be stress caused by low precipitation (Figure 5e,f), whereas in regions of high AGB, it is more likely that the pixel will not have stress driven by lagged precipitation (Figure 5g,h).

In regions where increasing LST/T_{air} is strongly positively associated with VPD, indicating stress from air dryness, the underlying ecosystem attributes are elevation, species richness, soil water pH,
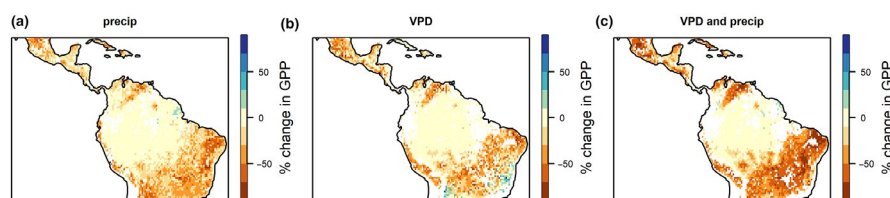
FIGURE 7 The percent change in gross primary production (GPP) when only precipitation is below its water stress threshold (a), when only vapor pressure deficit (VPD) is above its water stress threshold (b), and when both VPD and precipitation are crossing their critical thresholds (a compound event) (c)

AGB, soil silt content, CECC, and SOC. The top ecosystem attributes associated with VPD-caused vegetation stress are elevation (Figure 5i,j), which has varying effects depending on the ecosystem type, and species richness (Figure 5k,l), where the lower the species richness, the higher the probability of VPD-causing stress. For elevation, VPD-caused stress is most likely to occur between ~30 and 120 m (predominantly in the rainforest), and at very high elevations (>3000 m) in the mountains (Figure 5i,j).

3.3 | Critical thresholds and GPP

We found threshold values for stress caused by current and lagged precipitation are higher in the rainforest where average precipitation levels are greatest, and decrease in drier regions (Figure 6a–c), following the regional precipitation gradient. When precipitation is below its local threshold, we observed that GPP is reduced, for example, in the Cerrado and Caatinga regions of Brazil by as much as 70% (Figure 7a). Reductions of the same magnitude are also seen in Mexico, Central America, northern Venezuela, and Colombia. When precipitation stress is combined with high air dryness (Figure 7c), estimated GPP continues to decrease with up to an 80% decline compared to unstressed vegetation.

The critical threshold of <u>VPD</u> above which water stress is observed, that is the threshold at which a sharp increase of LST/T_{air} in response to VPD, tends to vary between 1.25 and 1.75 kPa across the Amazon basin (similar to current dry season values measured at 1:30 pm, the time of our VPD measurement), and increases to above 3 kPa in the Cerrado region (Figure 6d). This suggests that dryer regions are already acclimated to a higher VPD threshold for experiencing stress. Yet, when these thresholds are exceeded but rainfall remains plentiful, GPP remains unaffected or even increases in the rainforest regions of the southeastern Atlantic Forests (Figure 7b). In savanna and grassland regions to the southeast, as well as regions of Central America and northern Venezuela and Colombia, we observe the largest GPP reductions (up to 70%) when VPD surpasses its local threshold.

4 | DISCUSSION

Using the approach of combining remotely sensed changes of surface and air temperature with environmental drivers, we find that radiation best explains the temporal variability in LST/T_{air}, and hence of the surface energy balance throughout the study region (Figure 3e). Radiation increases LST/T_{air} directly, as surfaces and leaves tend to warm faster than the surrounding air. Too much direct radiation can be harmful to vegetation and increases leaf temperature, causing the production of toxic photo-oxidative intermediates (Foyer et al., 1994), or simply increasing the temperature of the leaf to above its optimum threshold for photosynthesis. Alternatively, an increased fraction of shortwave diffuse light decreases LST/T_{air} (Figure 3b). At the same level of light, diffuse light penetrates deeper through canopies (Mercado et al., 2009), especially thick canopies of tropical forests, reducing top of canopy heating and leading to higher rates of ecosystem transpiration in those energy-limited ecosystems (Bateni & Entekhabi, 2012).

The total effect of radiation (from both the diffuse fraction and R_n) on the temporal variation of LST/T_{air} is spatially widespread (Figure 3e), but was shown to be strongest in high AGB or high elevation regions (Figure 5a–d). In mountainous regions, primarily the Andes, an increasing fraction of diffuse light reduces LST/T_{air} (Figure 3a,b). At higher altitudes, there is less atmospheric optical depth, and thus, a higher direct light intensity which is frequently in excess to what is preferable for photosynthetic activity (Streb & Cornic, 2012). Thus, a higher fraction of diffuse light is favorable for photosynthesis and transpiration.

Regions where LST/T_{air} increases with radiation, in the Amazon, Atlantic Rainforests, and Central American forests, are associated with higher AGB (or canopy height). In these forests, satellite LST measurements only sense leaves in the top of the canopy, where top leaves can be up to 4°C warmer than the understory (Miller et al., 2021). The top leaves are largely light saturated, have lower light-use efficiency than the understory (Mercado et al., 2009), and can suffer from thermic stress in response to excessive light (Foyer et al., 1994). Here, an increase in the fraction of diffuse light (rather than direct) can improve the top of the canopy light-use efficiency, and may help sustain higher rates of transpiration in the overstory and the understory (Mercado et al., 2009).

In contrast to regions regulated by radiation, the effects of dry soil (lagged precipitation) most strongly increase LST/T_{air} in the water-limited regions of the Cerrado and Caatinga in Brazil (Figure 3c,f), which also have lower AGB and species richness. High species richness (overlapping with many of the high AGB regions of South America) tends to result in a greater diversity of plant hydraulic traits, and thus potentially greater resilience to drought (Anderegg et al., 2018). Thus, these dryer regions with lower species richness have increased sensitivity to water supplied by precipitation (Anderegg et al., 2018). When LST/T_{air} indicates that there is water stress from lower precipitation, carbon uptake is consistently reduced in these regions (Figure 7a).

Despite the Amazon rainforest being largely light limited (McVicar et al., 2012), some regions exhibit stress driven by air dryness (Figure 3d,g). These wet forest regions are exposed on average to lower VPD than the surrounding savanna and grassland, but also seem to be acclimated to a smaller range of air dryness. This is shown by their low VPD thresholds and high precipitation thresholds relative to other regions (Figure 6), making them more susceptible to even modest VPD increases falling outside these limited ranges to which they are acclimated. In fact, the stress thresholds for VPD in rainforests tend to hover around the mean VPD value measured at 1:30 pm local time in the dry season (~1.2–1.4 kPa); photosynthesis and thus transpiration can be reduced during these hours of peak sunlight and temperature in order to conserve water (Fig. S4). Within the rainforest, the regions with the strongest sensitivity to VPD lie at lower elevations (Figure 5i,j), which have greater soil moisture

and greater access to groundwater (e.g., from partial inundation). In these low-lying environments, we explain the vegetation sensitivity to VPD by the fact that plants acclimated to plentiful soil water supplies have developed lower resistance to xylem embolism (Oliveira et al., 2019; Signori-Müller et al., 2021), and are thus sensitive to VPD increases, since (partial) stomatal closure occurs at high VPD, causing a rise of LST/T_{air}.

However, unlike other regions, our results show that the VPD-caused increases of LST/T_{air} in the Amazon Rainforest do not necessarily translate into a decrease of *GPP* (Figure 7b), and that photosynthesis is instead likely to be maintained or increased. This phenomenon may be explained by seasonal leaf phenology and age. In the wettest areas of the Amazon rainforest, the dry season (when VPD and radiation are at their highest) coincides with the period of year when young leaves with high photosynthetic capacity are re-placing older leaves that are being shed at the top of the canopy (Asner & Alencar, 2010; Lopes et al., 2016). In a year without drought, the higher photosynthetic capacity of the new young leaves at the top of the canopy compensates for dry season GPP reductions from partial stomatal closure in response to high VPD and radiation during midday and afternoon (Green et al., 2020; Lopes et al., 2016; Wu et al., 2016). The VPD data used here are from 1:30 pm local time and reflect some of the highest VPD and radiation values for the full day. In fact, when looking at the average diurnal cycle for a flux tower site near Manaus, we see that the peak ET and GPP values occur around midday and then start to decline, while VPD in the dry season continues to increase in the afternoon (Fig. S4). Thus, while partial stomatal closure is being induced prior to the hours of peak atmospheric dryness and sunlight (as detected by the LST/T_{air} indicator), GPP reductions from this process appear to be compensated for by the higher photosynthetic capacity of the young leaves in the morning hours when *ViPD* levels are lower (Lin et al., 2019).

The influence of VPD on LST/T_{air} is also influenced by low species richness in drier savanna regions such as in the southeastern section of the study region and in Mexico (Figure 5k,l). Interestingly,

C4 sugarcane plantations and degraded forests with very low species richness are common in the Southern Brazilian regions where we see strong VPD sensitivity of LST/T_{air}, and in the most eastern section of the continent between the Caatinga region and the Atlantic Ocean. Yet, in those dry areas, VPD values above the critical threshold do not necessarily translate to a drop in GPP (Figure 7b). Sugarcane is a C4 species with higher photosynthetic efficiency compared to C3 species relating to photorespiration (Ghannoum, 2009), and even when canopy conductance is reduced in response to dryness, the vegetation has some ability to continue photosynthesizing under limited concentrations of intercellular CO_2. However, many of these drier regions are also sensitive to soil moisture deficits, which do in fact cause drops in GPP even when VPD values are below their critical thresholds (Figure 7a).

While the inclusion of ecosystem attributes such as AGB and species richness in our RF models allows the separation between regions that are water limited from regions that tend to be light limited (McVicar et al., 2012), the separation of regions mostly con-strained by (lagged) precipitation versus VPD limitation using soil and vegetation attributes is less distinguishable. This is due to the strong anticorrelation between precipitation and VPD due to land-atmosphere feedbacks (Zhou, Williams, et al., 2019; Zhou, Zhang, et al., 2019). For instance, as VPD increases, it will end up having a direct drying effect on the soil which can reduce precipitation in regions of high moisture recycling. Simultaneously, low soil moisture from minimal precipitation will contribute to increased VPD due to decreased ET. Nevertheless, despite the interactions between these stressors, we did find that the variability of rainfall events (quantified using the standard deviation of precipitation as an additional predic-tor in the regional random forest models) can assist in distinguishing between regions most sensitive to soil water supply versus air dry-ness. Regions with larger variability in precipitation (i.e., large sea-sonal changes) are more likely to exhibit a stronger stress response to soil water supply rather than air dryness (Fig. S5). These regions with strong seasonal changes in rainfall are in the Brazilian Cerrado,

(a) 2011–2019 clim

(b) clim anom 2015

(c) clim anom 2016

(d) clim anom 2019
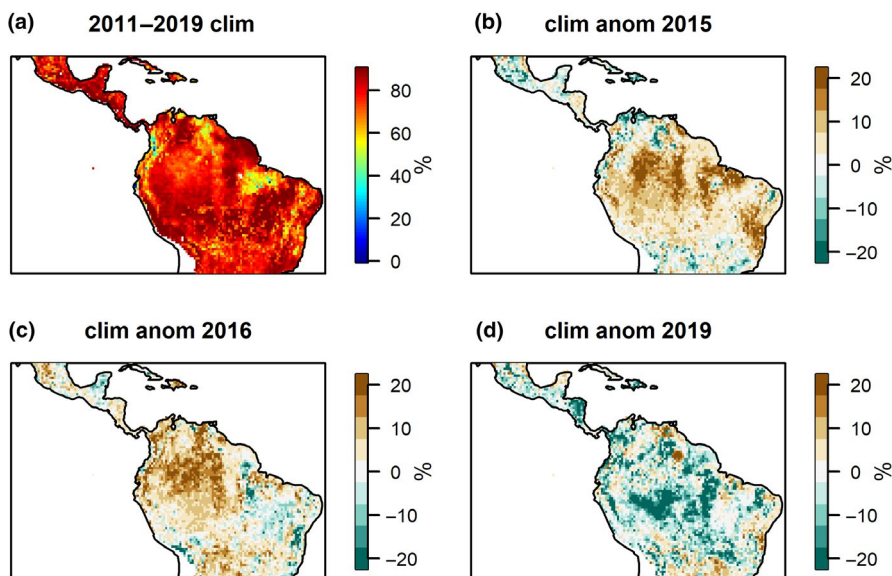
FIGURE 8 The percentage of variability in land surface temperature versus near surface air temperature (LST/T_{air}) explained by the pixelwise random forest models using Shapley values (Equations 4 and 5) for only climatological variables [the sum of net radiation (R_n), fraction of shortwave diffuse light, current and lagged precipitation, vapor pressure deficit (VPD), wind, and the climatology of contiguous solar-induced fluorescence (CSIF)] and no land cover data in 2011–2019 (a). The Shapley value climate anomaly (reflected as a percent change from the mean) of this same summation using only data from the year 2015 (b), 2016 (c), and 2019 (d)

a region that experiences several months each year with very low rainfall, leading to low soil moisture, causing vegetation to become soil water-limited.

While the surface energy budget of many regions responds primarily to only one environmental driver (Figure 5), there are also areas where vegetation stress is affected by multiple drivers, typically located along a climatic moisture gradient, or in a region that has shifted ecosystem types due to land cover change or degradation (Figure 2b). Additionally, multiple drivers can be due to seasonal changes in stress (e.g., dry season vs. wet season), changes in stress due to extreme events, such as droughts, or simply multiple stresses co-occurring (e.g., a compound event such as a drought and a heatwave together). For example, in the Amazon rainforest, certain pixels are impacted by both radiation and VPD, demonstrating that while this forest is typically light limited during the wet season due to high rainfall and humidity, during drier air conditions (i.e., seasonal or interannual droughts or dry season afternoons), increased atmospheric demand causes stomatal closure to preserve leaf water potential, resulting in LST/T_{air} increases. Additionally, in the Caatinga and Mexico regions, lagged precipitation and VPD simultaneously cause stress, as both soil moisture and VPD reduce leaf water potential and stomatal conductance, or cause nonstomatal limitations on photosynthesis, such as reductions in the maximum rate of carboxylation or mesophyll conductance. In these regions if either lagged precipitation stress or VPD stress occurs separately, there is a reduction in GPP (Figure 7a,b). However, when the two stressors coincide, the reduction of GPP is stronger (Figure 7c; Zhou, Williams, et al., 2019; Zhou, Zhang, et al., 2019), with daily GPP dropping by up to 80%. This indicates that atmospheric and soil water stress can interact synergistically to impact ecosystems and their carbon uptake (Zhou et al., 2019).

5 | CONCLUSIONS

These results demonstrate the utility of using temperature information, here using a stress index defined as LST/T_{air}, with machine learning approaches to detect vegetation stress, attribute this stress to environmental drivers, and identify ecosystem attributes that may enhance or diminish the impact of this stress. This new methodology can be extended to investigate the role of interannual variability, such as El Niño events, or disturbances on surface energy fluxes. For instance, our results show that during the El Niño years of 2015 and 2016, the fraction of variability in LST/T_{air} explained by environmental drivers related to climate (R_n, fraction of diffuse light, VPD, lagged precipitation, wind, and the climatology of CSIF) was greater than for the mean climatological year due to increased stress in these regions caused by strong temperature and precipitation anomalies (Figure 8a–c). We also see that in 2019, a year with an anomalously large number of fires that stemmed from anthropogenic sources rather than climatic drivers, the fraction of variability explained by the environmental drivers diminished (Figure 8d; Kelley et al., 2020).

As environmental conditions continue to change due to anthropogenic activity, both directly (e.g., fires, land cover change) and indirectly through emissions (e.g., warming, drying), understanding when and how vegetation is becoming stressed, as well as quantifying the thresholds that cause stress, become increasingly important. Here, we have identified thresholds in LST/T_{air} response to environmental drivers governed by AGB and species richness, two of the main ecosystem attributes affected by forest degradation and deforestation, suggesting that human land use has the potential to cause shifts in the surface energy budget throughout the Amazon (Loarie et al., 2011). Precipitation and *VPD* are also becoming more decoupled in the future, so that separating their relative influences becomes more essential to understand ecosystem response to climate change. The land surface plays a key role in global carbon and water cycles, by mitigating a large fraction of carbon emissions, reducing runoff, transpiring water to the atmosphere, and providing ecosystem services to humans and other species. The new diagnostic approach we have developed can be used in combination with other tools to monitor the health and function of different biomes at the global scale, thus providing an integrated assessment of vegetation water stress, necessary to monitor ecosystem health.

CONFLICT OF INTEREST
The authors declare no conflicts of interest.

DATA AVAILABILITY STATEMENT
All datasets used in this study are freely available from the following sources:

- Land surface temperature: https://land.copernicus.eu/global/products/lst

- Surface air temperature: https://disc.gsfc.nasa.gov/datasets/AIRS3STD_7.0/summary?keywords=airs%20version%207
- Contiguous solar induced fluorescence: https://osf.io/8xqy6/
- Precipitation: https://disc.gsfc.nasa.gov/datasets/TRMM_3B42_Daily_7/summary
- Net and fraction of diffuse radiation: https://ceres-tool.larc.nasa.gov/ord-tool/jsp/SYN1degEd41Selection.jsp
- Land cover change: https://search.earthdata.nasa.gov/search/granules?p=C203669657-LPDAAC_ECS&pg[0][gsk]=-start_date&q=MCD12C1&tl=1624901466.831!3!!
- Wind: https://cds.climate.copernicus.eu/cdsapp#!/dataset/reanalysis-era5-pressure-levels?tab=form
- Soil characteristics: https://daac.ornl.gov/cgi-bin/dsviewer.pl?ds_id=1247
- Elevation: https://www.eea.europa.eu/data-and-maps/data/world-digital-elevation-model-etopo5
- Species richness: http://ecotope.org/anthromes/biodiversity/plants/data/
- Aboveground biomass: https://drive.google.com/drive/folders/1mEiUi27-Mr0Hryrxvm2no70xqgZys0M?usp=sharing
- GPP: https://www.fluxcom.org/CF-Download/

The data used to generate the maps of variable importance (Figure 3) and critical thresholds (Figure 6) can be found here: https://doi.org/10.6078/D19M6J. All other modeled and calculated output (random forest model and Shapley value results) that support the findings of this study and computer code for data analyses are available from the corresponding author upon reasonable request (jgreen17@berkeley.edu).

ORCID

Julia K. Green https://orcid.org/0000-0002-8466-2313
Ashley Ballantyne https://orcid.org/0000-0003-1532-5126
Rose Abramoff https://orcid.org/0000-0002-3393-3064
Pierre Gentine https://orcid.org/0000-0002-0845-8345
David Makowski https://orcid.org/0000-0001-6385-3703
Philippe Ciais https://orcid.org/0000-0001-8560-4943

REFERENCES

Anderegg, W. R. L., Konings, A. G., Trugman, A. T., Yu, K., Bowling, D. R., Gabbitas, R., Karp, D. S., Pacala, S., Sperry, J. S., Sulman, B. N., & Zenes, N. (2018). Hydraulic diversity of forests regulates ecosystem resilience during drought. *Nature*, 561(7724), 538–541. https://doi.org/10.1038/s41586-018-0539-7

Aragão, L. E. O. C., Malhi, Y., Roman-Cuesta, R. M., Saatchi, S., Anderson, L. O., & Shimabukuro, Y. E. (2007). Spatial patterns and fire response of recent Amazonian droughts. *Geophysical Research Letters*, 34(7), 1–5. https://doi.org/10.1029/2006GL028946

Asner, G. P., & Alencar, A. (2010). Drought impacts on the Amazon forest: The remote sensing perspective. *The New Phytologist*, 187(3), 569–578. https://doi.org/10.1111/j.1469-8137.2010.03310.x

Bateni, S. M., & Entekhabi, D. (2012). Relative efficiency of land surface energy balance components. *Water Resources Research*, 48(4), 1–8. https://doi.org/10.1029/2011WR011357

Breiman, L. (2001). Random forests. *Machine Learning*, 45, 5–32. https://doi.org/10.1201/9780367816377-11

Dee, D. P., Uppala, S. M., Simmons, A. J., Berrisford, P., Poli, P., Kobayashi, S., Andrae, U., Balmaseda, M. A., Balsamo, G., Bauer, P., Bechtold, P., Beljaars, A. C. M., van de Berg, L., Bidlot, J., Bormann, N., Delsol, C., Dragani, R., Fuentes, M., Geer, A. J., … Vitart, F. (2011). The ERA-Interim reanalysis: Configuration and performance of the data assimilation system. *Quarterly Journal of the Royal Meteorological Society*, 137(656), 553–597. https://doi.org/10.1002/qj.828

Ellis, E. C., Antill, E. C., & Kreft, H. (2012). All is not loss: Plant biodiversity in the anthropocene. *PLoS One*, 7(1), e30535. https://doi.org/10.1371/journal.pone.0030535

Entekhabi, D., Yueh, S. I., O'Neil, P. E., Kellogg, K. H., Allen, A., Bindlish, R.; National Aeronautics and Space Administration. (2014). *SMAP handbook soil moisture active passive mapping soil moisture and freeze/thaw from space*. National Aeronautics and Space Administration.

Fan, Y., Miguez-Macho, G., Jobbágy, E. G., Jackson, R. B., & Otero-Casal, C. (2017). Hydrologic regulation of plant rooting depth. *Proceedings of the National Academy of Sciences*, 114(40), 10572–10577. https://doi.org/10.1073/pnas.1712381114

FAO/IIASA/ISRIC/ISSCAS/JRC. (2012). Harmonized world soil database. FAO, Rome, Italy and IIASA, Laxenburg, Austria.

Farquhar, G. D., & Cowan, I. R. (1977). Stomatal function in relation to leaf metabolism and environment. In D. H. Jennings (Ed.), *Integration of activity in the higher plant* (pp. 471–505). Cambridge University Press.

Feldman, A. F., Short Gianotti, D. J., Trigo, I. F., Salvucci, G. D., & Entekhabi, D. (2019). Satellite-based assessment of land surface energy partitioning-soil moisture relationships and effects of confounding variables. *Water Resources Research*, 55(12), 10657–10677. https://doi.org/10.1029/2019WR025874

Foyer, C. H., Lelandais, M., & Kunert, K. J. (1994). Photooxidative stress in plants. *Physiologia Plantarum*, 92, 696–717. https://doi.org/10.1111/j.1399-3054.1994.tb03042.x

Friedl, M. A., & Sulla-Menashe, D. (2018). User guide to collection 6 MODIS land cover (MCD12Q1 and MCD12C1) product. User guide, figure 1, 1–18. https://doi.org/10.5067/MODIS/MCD12Q1.006

Friedlingstein, P., O'Sullivan, M., Jones, M. W., Andrew, R. M., Hauck, J., Olsen, A., Peters, G. P., Peters, W., Pongratz, J., Sitch, S., Le Quéré, C., Canadell, J. G., Ciais, P., Jackson, R. B., Alin, S., Aragão, L. E. O. C., Arneth, A., Arora, V., Bates, N. R., … Zaehle, S. (2020). Global carbon budget 2020. *Earth System Science Data*, 12(4), 3269–3340. https://doi.org/10.5194/essd-12-3269-2020

Gentine, P., Chhang, A., Rigden, A., & Salvucci, G. (2016). Evaporation estimates using weather station data and boundary layer theory. *Geophysical Research Letters*, 43(22), 11661–11670. https://doi.org/10.1002/2016GL070819

Ghannoum, O. (2009). C4 photosynthesis and water stress. *Annals of Botany*, 103(4), 635–644. https://doi.org/10.1093/aob/mcn093

Giardina, F., Konings, A. G., Kennedy, D., Alemohammad, S. H., Oliveira, R. S., Uriarte, M., & Gentine, P. (2018). Tall Amazonian forests are less sensitive to precipitation variability. *Nature Geoscience*, 11(6), 405–409. https://doi.org/10.1038/s41561-018-0133-5

Good, E. J. (2016). An in situ-based analysis of the relationship between land surface "skin" and screen-level air temperatures. *Journal of Geophysical Research*, 121(15), 8801–8819. https://doi.org/10.1002/2016JD025318

Green, J. K., Berry, J., Ciais, P., Zhang, Y., & Gentine, P. (2020). Amazon rainforest photosynthesis increases in response to atmospheric dryness. *Science Advances*, 6, eabb7232. https://doi.org/10.1126/sciadv.abb7232

Green, J. K., Seneviratne, S. I., Berg, A. M., Findell, K. L., Hagemann, S., Lawrence, D. M., & Gentine, P. (2019). Large influence of soil moisture on long-term terrestrial carbon uptake. *Nature*, 565(7740), 476–479. https://doi.org/10.1038/s41586-018-0848-x

Greenwell, B. M. (2017). pdp: An R package for constructing partial dependence plots. *R Journal*, *9*(1), 421–436. https://doi.org/10.32614/rj-2017-016

Greenwell, B. (2020). Fastshap: Fast approximate shapley values. https://cran.r-project.org/package=fastshap

Greenwell, B. M., Boehmke, B. C., & McCarthy, A. J. (2018). A simple and effective model-based variable importance measure. 1–27. http://arxiv.org/abs/1805.04755

Guyon, I., Weston, J., Barnhill, S., & Vapnik, V. (2002). Gene selection for cancer classification using Support Vector Machines. *Machine Learning*, *46*, 389–422. https://doi.org/10.1007/978-3-540-88192-6_8

Hart, S. (1989). Shapley value. In J. Eatwell, M. Milgate, & P. Newman (Eds.), *Game theory* (pp. 210–216). Palgrave Macmillan. https://doi.org/10.1007/978-1-349-20181-5_25

Holmgren, M., Hirota, M., Van Nes, E. H., & Scheffer, M. (2013). Effects of interannual climate variability on tropical tree cover. *Nature Climate Change*, *3*(8), 755–758. https://doi.org/10.1038/nclimate1906

Huete, A. R., Liu, H. Q., & van Leeuwen, W. J. D. (1997). Use of vegetation indices in forested regions: Issues of linearity and saturation. *International Geoscience and Remote Sensing Symposium (IGARSS)*, *4*(January 2016), 1966–1968. https://doi.org/10.1109/igarss.1997.609169

Huffman, G. J., Adler, R. F., Bolvin, D. T., Gu, G., Nelkin, E. J., Bowman, K. P., Hong, Y., Stocker, E. F., & Wolff, D. B. (2007). The TRMM multisatellite precipitation analysis (TMPA): Quasi-global, multiyear, combined-sensor precipitation estimates at fine scales. *Journal of Hydrometeorology*, *8*(1), 38–55. https://doi.org/10.1175/JHM560.1

Humphrey, V., Berg, A., Ciais, P., Gentine, P., Jung, M., Reichstein, M., Seneviratne, S. I., & Frankenberg, C. (2021). Soil moisture–atmosphere feedback dominates land carbon uptake variability. *Nature*, *592*(7852), 65–69. https://doi.org/10.1038/s41586-021-03325-5

Jung, M., Schwalm, C., Migliavacca, M., Walther, S., Camps-Valls, G., Koirala, S., Anthoni, P., Besnard, S., Bodesheim, P., Carvalhais, N., Chevallier, F., Gans, F., Goll, D. S., Haverd, V., Köhler, P., Ichii, K., Jain, A. K., Liu, J., Lombardozzi, D., … Reichstein, M. (2020). Scaling carbon fluxes from eddy covariance sites to globe: Synthesis and evaluation of the FLUXCOM approach. *Biogeosciences*, *17*(5), 1343–1365. https://doi.org/10.5194/bg-17-1343-2020

Kelley, D., Burton, C., Huntingford, C., Brown, M., Whitley, R., & Dong, N. (2020). Technical note: Low meteorological influence found in 2019 Amazonia fires. *Biogeosciences Discussions*, *May*, 1–17. https://doi.org/10.5194/bg-2020-123

Lian, X., Zeng, Z., Yao, Y., Peng, S., Wang, K., & Piao, S. (2017). Spatiotemporal variations in the difference between satellite-observed daily maximum land surface temperature and station-based daily maximum near-surface air temperature. *Journal of Geophysical Research*, *122*(4), 2254–2268. https://doi.org/10.1002/2016JD025366

Lin, C., Gentine, P., Frankenberg, C., Zhou, S., Kennedy, D., & Li, X. (2019). Evaluation and mechanism exploration of the diurnal hysteresis of ecosystem fluxes. *Agricultural and Forest Meteorology*, *278*, 107642. https://doi.org/10.1016/j.agrformet.2019.107642

Liu, L., Gudmundsson, L., Hauser, M., Qin, D., Li, S., & Seneviratne, S. I. (2020). Soil moisture dominates dryness stress on ecosystem production globally. *Nature Communications*, *10*(3), 247–249. https://doi.org/10.1134/S1995082917030038

Loarie, S. R., Lobell, D. B., Asner, G. P., Mu, Q., & Field, C. B. (2011). Direct impacts on local climate of sugar-cane expansion in Brazil. *Nature Climate Change*, *1*(2), 105–109. https://doi.org/10.1038/nclimate1067

Long, D., Longuevergne, L., & Scanlon, B. R. (2014). Uncertainty in evapotranspiration from land surface modeling, remote sensing, and GRACE satellites. *Water Resources Research*, *50*(2), 1131–1151. https://doi.org/10.1002/2013WR014581

Lopes, A. P., Nelson, B. W., Wu, J., Graça, P. M. L. D. A., Tavares, J. V., Prohaska, N., Martins, G. A., & Saleska, S. R. (2016). Leaf flush drives dry season green-up of the Central Amazon. *Remote Sensing of Environment*, *182*, 90–98. https://doi.org/10.1016/j.rse.2016.05.009

Martins, J. P., Trigo, I., & Freitas, S. C. E. (2020). Copernicus global land operations " vegetation and energy" "CGLOPS-1." In *Copernicus Global Land Operations*. https://land.copernicus.eu/global/products/lai

McKee, T. B., Doesken, N. J., & Kleis, J. (1993). The relationship of drought frequency and duration to time scales. *Eighth Conference on Applied Climatology*. https://doi.org/10.1002/jso.23002

McVicar, T. R., Roderick, M. L., Donohue, R. J., Li, L. T., Van Niel, T. G., Thomas, A., Grieser, J., Jhajharia, D., Himri, Y., Mahowald, N. M., Mescherskaya, A. V., Kruger, A. C., Rehman, S., & Dinpashoh, Y. (2012). Global review and synthesis of trends in observed terrestrial near-surface wind speeds: Implications for evaporation. *Journal of Hydrology*, *416–417*, 182–205. https://doi.org/10.1016/j.jhydrol.2011.10.024

Mercado, L. M., Bellouin, N., Sitch, S., Boucher, O., Huntingford, C., Wild, M., & Cox, P. M. (2009). Impact of changes in diffuse radiation on the global land carbon sink. *Nature*, *458*(7241), 1014–1017. https://doi.org/10.1038/nature07949

Miller, B. D., Carter, K. R., Reed, S. C., Wood, T. E., & Cavaleri, M. A. (2021). Only sun-lit leaves of the uppermost canopy exceed both air temperature and photosynthetic thermal optima in a wet tropical forest. *Agricultural and Forest Meteorology*, *301–302*, 108347. https://doi.org/10.1016/j.agrformet.2021.108347

Oliveira, R. S., Costa, F. R. C., Baalen, E., Jonge, A., Bittencourt, P. R., Almanza, Y., Barros, F. D. V., Cordoba, E. C., Fagundes, M. V., Garcia, S., Guimaraes, Z. T. M., Hertel, M., Schietti, J., Rodrigues-Souza, J., & Poorter, L. (2019). Embolism resistance drives the distribution of Amazonian rainforest tree species along hydro-topographic gradients. *New Phytologist*, *221*(3), 1457–1465. https://doi.org/10.1111/nph.15463

Pan, Y., Birdsey, R. A., Fang, J., Houghton, R., Kaupii, P. E., Kurz, W. A., Phillips, O. L., Shvidenko, A., Lewis, S. L., Canadell, J. G., Ciais, P., Jackson, R. B., Pacala, S. W., McGuire, D. A., Piao, S., Rautiained, A., Sitch, S., & Hayes, D. (2011). A large and persistent carbon sink. *Science*, *333*(August), 988–993.

Qiu, J., Crow, W. T., & Nearing, G. S. (2016). The impact of vertical measurement depth on the information content of soil moisture for latent heat flux estimation. *Journal of Hydrometeorology*, *17*(9), 2419–2430. https://doi.org/10.1175/JHM-D-16-0044.1

Quesada, C. A., Lloyd, J., Schwarz, M., Patiño, S., Baker, T. R., Czimczik, C., Fyllas, N. M., Martinelli, L., Nardoto, G. B., Schmerler, J., Santos, A. J. B., Hodnett, M. G., Herrera, R., Luizão, F. J., Arneth, A., Lloyd, G., Dezzeo, N., Hilke, I., Kuhlmann, I., … Paiva, R. (2010). Variations in chemical and physical properties of Amazon forest soils in relation to their genesis. *Biogeosciences*, *7*(5), 1515–1541. https://doi.org/10.5194/bg-7-1515-2010

Quesada, C. A., Phillips, O. L., Schwarz, M., Czimczik, C. I., Baker, T. R., Patiño, S., Fyllas, N. M., Hodnett, M. G., Herrera, R., Almeida, S., Alvarez Dávila, E., Arneth, A., Arroyo, L., Chao, K. J., Dezzeo, N., Erwin, T., di Fiore, A., Higuchi, N., Honorio Coronado, E., … Lloyd, J. (2012). Basin-wide variations in Amazon forest structure and function are mediated by both soils and climate. *Biogeosciences*, *9*(6), 2203–2246. https://doi.org/10.5194/bg-9-2203-2012

Rodell, M., Houser, P. R., Jambor, U., Gottschalck, J., Mitchell, K., Meng, C.-J., Arsenault, K., Cosgrove, B., Radakovich, J., Bosilovich, M., Entin, J. K., Walker, J. P., Lohmann, D., & Toll, D. (2004). The global land data assimilation system. *Bulletin of the American Meteorological Society*, *85*(3), 381–394. https://doi.org/10.1175/BAMS-85-3-381

Saatchi, S. S., Harris, N. L., Brown, S., Lefsky, M., Mitchard, E. T. A., Salas, W., Zutta, B. R., Buermann, W., Lewis, S. L., Hagen, S., Petrova, S., White, L., Silman, M., & Morel, A. (2011). Benchmark

map of forest carbon stocks in tropical regions across three continents. *Proceedings of the National Academy of Sciences of the United States of America, 108*(24), 9899–9904. https://doi.org/10.1073/pnas.1019576108

Seneviratne, S. I., Donat, M. G., Mueller, B., & Alexander, L. V. (2014). No pause in the increase of hot temperature extremes. *Nature Climate Change, 4*(3), 161–163. https://doi.org/10.1038/nclimate2145

Signori-Müller, C., Oliveira, R. S., Barros, F. D. V., Tavares, J. V., Gilpin, M., Diniz, F. C., Zevallos, M. J. M., Yupayccana, C. A. S., Acosta, M., Bacca, J., Chino, R. S. C., Cuellar, G. M. A., Cumapa, E. R. M., Martinez, F., Mullisaca, F. M. P., Nina, A., Sanchez, J. M. B., da Silva, L. F., Tello, L., … Galbraith, D. (2021). Non-structural carbohydrates mediate seasonal water stress across Amazon forests. *Nature Communications, 12*(1), 1–9. https://doi.org/10.1038/s41467-021-22378-8

Sörensson, A. A., & Ruscica, R. C. (2018). Intercomparison and uncertainty assessment of nine evapotranspiration estimates over South America. *Water Resources Research, 54*(4), 2891–2908. https://doi.org/10.1002/2017WR021682

Souza, A. G. S. S., Neto, A. R., Rossato, L., Alvalá, R. C. S., & Souza, L. L. (2018). Use of SMOS L3 soil moisture data: Validation and drought assessment for Pernambuco State, Northeast Brazil. *Remote Sensing, 10*(8), 1–19. https://doi.org/10.3390/RS10081314

Spawn, S. A., & Gibbs, H. K. (2020). Global aboveground and belowground biomass carbon density maps for the year 2010. *ORNL DAAC*. https://doi.org/10.3334/ORNLDAAC/1763

Streb, P., & Cornic, G. (2012). Photosynthesis and antioxidative protection in alpine herbs. In C. Lütz (Ed.), *Plants in Alpine regions: Cell physiology of adaptation and survival strategies* (pp. 75–97). Springer.

Teixeira, A. S. T. (2013). *AIRS/Aqua L3 monthly standard physical retrieval (AIRS+AMSU) 1 degree x 1 degree V006*. Goddard Earth Sciences Data and Information Services Center (GES DISC). https://doi.org/10.5067/Aqua/AIRS/DATA319

Wieder, W. R., Boehnert, J., Bonan, G. B., & Langseth, M. (2014). *Regridded Harmonized world soil database v1.2*. Oak Ridge National Laboratory Distributed Active Archive Center. https://doi.org/10.3334/ORNLDAAC/1247

Wielicki, B. A., Barkstrom, B. R., Harrison, E. F., Lee, R. B., Smith, G. L., & Cooper, J. E. (1996). Clouds and the Earth's Radiant Energy System (CERES): An earth observing system experiment. *Bulletin of the American Meteorological Society, 77*(5), 853–868. https://doi.org/10.1175/1520-0477(1996)077<0853:CATERE>2.0.CO;2

Wright, M. N., & Ziegler, A. (2017). Ranger: A fast implementation of random forests for high dimensional data in C++ and R. *Journal of Statistical Software, 77*(1), 1–17. https://doi.org/10.18637/jss.v077.i01

Wu, J., Albert, L. P., Lopes, A. P., Restrepo-Coupe, N., Hayek, M., Wiedemann, K. T., Guan, K., Stark, S. C., Christoffersen, B., Prohaska, N., Tavares, J. V., Marostica, S., Kobayashi, H., Ferreira, M. L., Campos, K. S., da Silva, R., Brando, P. M., Dye, D. G., Huxman, T. E., … Saleska, S. R. (2016). Leaf development and demography explain photosynthetic seasonality in Amazon evergreen forests. *Science, 351*(6276), 972–976. https://doi.org/10.1126/science.aad5068

Wuertz, D. (2020). *timeSeries: Financial time series objects (Rmetrics)*. R package (R package version 3062.100.).

Yang, X., Post, W. M., Thornton, P. E., & Jain, A. (2013). The distribution of soil phosphorus for global biogeochemical modeling. *Biogeosciences, 10*(4), 2525–2537. https://doi.org/10.5194/bg-10-2525-2013

Zhang, Y., Joiner, J., Alemohammad, S. H., Zhou, S., & Gentine, P. (2018). A global spatially Continuous Solar Induced Fluorescence (CSIF) dataset using neural networks. *Biogeosciences Discussions*, June, 1–34. https://doi.org/10.5194/bg-2018-255

Zhou, S., Williams, A. P., Berg, A. M., Cook, B. I., Zhang, Y., Hagemann, S., Lorenz, R., Seneviratne, S. I., & Gentine, P. (2019). Land–atmosphere feedbacks exacerbate concurrent soil drought and atmospheric aridity. *Proceedings of the National Academy of Sciences of the United States of America, 116*(38), 18848–18853. https://doi.org/10.1073/pnas.1904955116

Zhou, S., Zhang, Y., Williams, A. P., & Gentine, P. (2019b). Projected increases in intensity, frequency, and terrestrial carbon costs of compound drought and aridity events. *Science Advances, 5*(1), 1–9. https://doi.org/10.1126/sciadv.aau5740

SUPPORTING INFORMATION

Additional supporting information may be found in the online version of the article at the publisher's website.

How to cite this article: Green, J. K., Ballantyne, A., Abramoff, R., Gentine, P., Makowski, D., & Ciais, P. (2022). Surface temperatures reveal the patterns of vegetation water stress and their environmental drivers across the tropical Americas. *Global Change Biology*, 00, 1–16. https://doi.org/10.1111/gcb.16139